Please cite the Published Version

Additional Information: This is an Author Accepted Manuscript of a paper accepted for publication in Energy Storage Materials, published by and copyright Elsevier.

Enquiries:
If you have questions about this document, contact openresearch@mmu.ac.uk. Please include the URL of the record in e-space. If you believe that your, or a third party's rights have been compromised through this document please see our Take Down policy (available from https://www.mmu.ac.uk/library/using-the-library/policies-and-guidelines)

Binding MoSe$_2$ with carbon constrained in carbonous nanosphere towards High-Capacity and Ultrafast Li/Na-Ion Storage

Abstract:

Mostly reported MoSe$_2$ suffered from easily stacking problem, volume expansion and relative low capacity. From the experience of Li/Na-Se batteries, the exfoliated and encapsulated MoSe$_2$ inside carbon nanospheres with C-O-Mo bonds and large layer distance (0.89 nm) are successfully constructed. This unique effective structure has C-O-Mo bonding allowing high conductivity across the Se-O insulation layer and promoting its reversible conversion. The first-principles calculations demonstrated that the frontier molecular orbitals of C-O-Mo interface structure are mainly localized on the MoSe$_2$ sheet fragment with an appropriate HOMO-LUMO gap (< 4eV), suggesting its good stability and conductivity. Utilized as anodes for LIBs allows a Li-storage capacity to be realized of 1208 mAh g^{-1} after 150 cycles at 1.0 A g^{-1} and 519 mAh g^{-1} after 200 cycles at 4.0 A g^{-1}. The Na-storage capacity is found to be 543, 491 mAh g^{-1} after 120 cycles at 0.1, 1.0 A g^{-1}. Focusing on the analysis of CV, the reducing particle may improve the capacitive behaviors, further resulting the high-rate performance. *Ex-situ* techniques demonstrated that the emerging Se was constrained uniformly. The controlling of by-product Se plays a key role in achieving a high rate

capacity and cycling stability, and opens up a potential avenue for these metal-selenide anodes designs for battery storage systems.

Keywords: $MoSe_2$, *in-situ* generated Se, lithium ions battery, sodium ions battery, electrochemistry

1. Introduction

Recently, owing to the promising lithium/sodium-selenium batteries, metal-selenium have captured widespread interests.[1] Despite the cost of Se, its stable electrochemical reaction and less solubility are more valuable in practical application. $MoSe_2$, as a rising star in TMDCs family, possesses numerous primary advantages, containing narrowe band-gap (1.1 eV), large interlayer distances (0.65 nm) and high electronic conductivity (Se brings the metallic nature, $1 \times 10^{-3}S\ m^{-1}$), which could lower the energy-consumption of electron transition, increase the shuttling rate of alkali metal ions and thus reduce the electron transport resistance.[2] Based on the sole conversion reaction ($MoSe_2 + 4Li^+/Na^+ + 4e^- \rightarrow LiSe_2/NaSe_2 + Mo$), the theoretically capacity of $MoSe_2$ reaches to 422 mAh g^{-1}, but the exceeding Li/Na-storage capacity has been reported in the previous works by Tang et al. and Wang et al,[3, 4] demonstrating the potential of capacity as a promising anode within LIBs/SIBs. Nevertheless, for the metal-selenide materials, the large volume variation, inferior mechanical stress and relative low Na-storage capacity, were all major challenges.[1, 2] Two approaches were employed to address these issues, including

the engineering of morphology and introduction of carbon materials. Generally speaking, the reducing particles size is in favor of improving the contracting areas with the electrolyte, which could shorten the pathways of Li/Na diffusion, thereby giving rise to the increased rate capability.[5] Different morphologies of $MoSe_2$ with diverse sizes have been designed and their electrochemical properties were explored, such as the microsphere, yolk-shell structure, nanosheets and other special morphologies.[2] The $MoSe_2$ nanospheres have been obtained through a simple colloidal route, exhibiting a high initial discharge/charge capacity of 520/430 mAh g^{-1} when utilized as anodes within SIBs.[6] On the other hand, coupling $MoSe_2$ with carbon is deemed as the effective way to reduce the accumulated strain, control the volume expansion as well as ensure the fast alkali ions.[7] After the activated treatment of carbon nanotube/graphene, $MoSe_2$ could successfully grow upon the surface of substrate, accelerating the swelling of electrolyte and the shuttling of alkali ions.[8] Incorporating 1T-$MoSe_2$ with SWCNT into the conductive structure was prepared by Song's group,[9] delivering a capacity of 630 mAh g^{-1} at 3.0 A g^{-1}. However, similar to the deficient defects of MoS_2, that of $MoSe_2$ should be emphasized: (1) the Mo nanoparticles replaced by alkalis ions would largely agglomerate and move outward easily; (2) the dissolution of the *in-situ* generated selenide due to the weaker bonding force of Mo-Se than that of Mo-O/S could result in the rapid capacity fading.[10] The growth of $MoSe_2$ upon the conductivity substrate could lead to a large specific surface area of $MoSe_2$/graphene or nanotube exposed in

3

the electrolyte, accompanying with the deteriorated adverse reaction, whilst the Mo-containing ions and *in-situ* generated Se cannot be timely captured for the reverse process. All of the aforementioned drawbacks would bring the poor electrochemical properties of $MoSe_2$.

The rational design of $MoSe_2$/C is crucial for improving the Li/Na-storage abilities, including the enlarged interlayer spacing and the coated carbon layer-by-layer. For this purpose, the selected carbon sources could act as two roles: the exfoliated and covered agents. Taking into consideration of the liquid-phase reaction environment, non-ionic surfactant / polymer-assisted exfoliation methods should be emphasized owing to their additional stabilization and dispersing features.[11] Polyvinyl pyrrolidone (PVP), as one of nine non-ionic surfactants (*e.g.* Pluronic P-123, n-dodecyl b-dmaltoside), can be easily attached to the surface of $MoSe_2$ through strong adsorption forces, allowing this coated $MoSe_2$ to form hybrid nanosheets, originated from the well solubility and wetting properties.[12-15] Recent work displays the successful formation of PVP-coated $MoSe_2$ nanosheets utilized as biocompatible photothermal therapy agents.[13]

In this work, the nanospheres (diameter of 100 nm) composed of PVP-coated $MoSe_2$ nanosheets were prepared expectedly, after a carbonization process, allowing for the large interlayer distance, C-O-Mo bonds and layer-by-layer nitrogen-doped carbon heterostructure. Inspiringly, the obtained $MoSe_2$/N-C anode for LIBs delivers larger capacities of 769.7 and 273.2 mAh g^{-1} at 2.0 and 8.0 A g^{-1}, respectively.

Surprisingly, as anodes for SIBs, the prepared sample has an excellent reversible capacity of 552.1 mAh g^{-1} at 0.1 A g^{-1} after 120 cycles. Even at 2.0 and 8.0 A g^{-1}, it still remains at 441.7 and 236.4 mAh g^{-1} respectively. The high-capacity and ultrafast Li/Na-ion storage are mainly due to: (1) the open nanostructure enlarged connecting area with the electrolyte; (2) the expanded interlayer of MoSe$_2$ decreased the electron-shuttling resistance and increased the accessible active sites; (3) the *in-situ* generated selenium was effectively confined in the carbon substrate, which improves the Li/Na-storage capacity distinctly. In addition, the experimental and computational results consistently indicated the formation of the unique C-O-Mo bonds in the novel MoSe$_2$/C battery material, which would be beneficial to stabilizing the volume expansion and give a faster rate of electron transfer. Furthermore, the first-principles calculations predicted that the unique C-O-Mo bond should make the hybrid materials possess a superior general performance (good stability and excellent conductivity).

2. Experimental section

2.1 Synthesis of MoSe$_2$ hollow flower spheres (FMS) and MoSe$_2$/N-C (PMS) nanospheres

0.156 g Se and 0.156 g MoO$_3$ was added to 25 mL hydrazine hydrate, followed by 30 min magnetic stirring at 300 rpm to form solution A. 2.0 g NH$_4$F and 0.8 g PVP were dissolved in 50 mL deionized water (DI water), then 75mL ethanol was injected, with 30 min stirring to obtain solution B. Solution A was added drop-wise to solution B, the mixed solutions were stirred for 30 min at 600 rpm and further ultrasonicated for

1h. The final well-distributed solution was transferred to an autoclave and remained at 180 °C for 12 h. The autoclave was naturally cooled down to room temperature. The liquid suspension was centrifuged at 11000 rpm for 5 min and washed thoroughly with water and ethanol three times. The black products were dried at 80 °C and further calcined at 500 °C in the Ar atmosphere to obtained PMS nanospheres. Without the introduction of PVP, $MoSe_2$ hollow flower spheres through the same procedures were prepared, named FMS. The commercial $MoSe_2$ (Alpha) via the sintering process was named CMS.

2.2 Electrochemical Characterization:

The structure features were investigated through Power X-ray diffractometer (Rigaku D/max 2550 VB+18 kW, Japan), Laser Micro-Raman Spectrometer (Renishaw InVia, UK) and thermogravimetric analysis (TGA, NETZSCH STA449F3). X-ray photoelectron spectroscopy (XPS, K-Alpha 1063, UK) is used to analyze those chemical valences. The micro-morphologies were investigated through scanning electron microscopy (SEM, a JEM-2100F instrument at 200 kV) and Transmission electron (TEM, JEM-2100F).

2.3 Electrochemical Measurements.

The homogeneous slurry was obtained via mixing active materials, Super P (acetylene black), and hydroxymethyl cellulose (CMC) with a weight ratio of 80 : 10 : 10 in deionized water (DI water). After the doctor blading of the slurry on the Cu foil, it was dried in a vacuum oven at 60 °C for 10h. The metal (Li/Na) and the as-prepared

electrodes were assembled in the argon glovebox. The separator was Celgard2400 and the electrolyte was 1M $NaClO_4$ in propylene carbonate (PC) with 5% fluoroethylene carbonate (FEC) additive. The galvanostatic discharge/charge tests were performance on a Land CT 2001 battery and Arbin battery cycler (BT2000) between 0.01 and 3.0V. Utilizing the AUTOLABEL MULTI AUTOLAB M204 instruments under various conditions, the electrochemical impedimetric (EIS) and cyclic voltammetric (CV) measurements were explored.

2.4 First-principles Calculations

2.4.1 Simplified computational models

To balance the calculation accuracy and computational cost, the simplified computational cluster models of $MoSe_2$ sheet fragment and graphene fragment (C60 fullerene) are proposed to represent the $MoSe_2$ and carbon materials, respectively. The $MoSe_2$ sheet fragment is directly generated from the experimental crystal structure of $MoSe_2$, which contains five Mo atoms, and each Mo atom is coordinated by two Se atoms. Oxidized graphene fragment is prepared by running a full optimization calculation for a system in which an oxygen atom is placed onto the center of a simplified graphene fragment (pyrene). Similarly, oxidized C60 fullerene is obtained by optimizing a system in which an oxygen atom is placed on to a carbon atom of C60 crystal structure. Then, these well-prepared fragments (as displayed in Figure 3) were assembled to construct C-O-Mo interface models, which are further optimized to obtain C-O-Mo interface structures (as shown in Figure 3).

2.4.2 Computational details

All the first-principles calculations are performed by using the version D01 of Gaussian 09. Specifically, the state-of-the-art hybrid functional B3LYP and ωB97XD are adopted with basis set of 6-31G* on C, O atoms, and LanL2DZ with efficient core potential (ECP) on Mo and Se atoms. The LAN2DZ ECP for Mo replaces the innermost 28 electrons [$1s^2$ $2s^2p^6$ $3s^2p^6d^{10}$] in Mo by a relativistic ECP and treats the remaining 14 electrons [$4s^2p^6d^5$ $5s^1$] explicitly. Similarly, LAN2DZ ECP for Se replaces the innermost 28 electrons [$1s^2$ $2s^2p^6$ $3s^2p^6d^{10}$] in Se by a non-relativistic ECP and treats the remaining 6 electrons [$4s^2p^4$] explicitly. The proposed interface structures of C-O-Mo are restrictively optimized, only allowing the molybdenum, oxygen atoms (at bonding point) and two carbon atoms closest to the oxygen atom could move freely when optimization to mimic the rigid enviroment of crystal structure of MoSe$_2$ and carbon materials. B3LYP hybrid functionals have been proved to obtain reasonable geometry structures for a variety of transition metal systems, while ωB97XD functional is well known for their accuracy in electronic structure and thermochemistry.

3. Results and Discussions

The formation mechanism of PVP was clearly shown in Fig. 1a. PVP with excellent solubility and wetting properties are easily attached to the surface of MoSe$_2$, forming MoSe$_2$/PVP hybrid nanosheets.[15] Fig. 1b displays the FTIR spectrum of

MoSe$_2$/PVP and PVP. The peaks at 3434, 2955, 1661, 1290 cm^{-1} is the characteristic peaks of -OH, C-H, C=O, C-N stretching vibration, demonstrating the successful formation of MoSe$_2$/PVP.[12] The distinctions of the CMS/FMS/PMS structures are analyzed *via* the XRD patterns as shown in Fig. 1a. The high purity of all the samples are observed, indexing to those of hexagonal-phase (JCPDS Card No. 29-0914). For PMS, the crystallinity of these samples is gradually lowered in the order of CMC > FMS > PMS. The (002) peaks of them have been shifted towards lower angels in file CMC (13.68^o) > FMS (12.98^o) > PMS (10.0 ^{o}), suggesting the enlarged interlayer distance. According to Bragg's equation (2dsinθ = nλ),[16] the d(002) values are calculated to 0.65, 0.68 and 0.87 nm, respectively. Furthermore, the grain sizes (D$_{hkl}$) of FMS/PMS are 3.6, 3.4 nm through the utilization of the Scherrer's equation (D$_{hkl}$=Kλ/βcosθ).[16] And the number of interlayers (D$_{hkl}$/d(002) is 5.3 (3.6/0.68) and 3.9 (3.4/0.89)), confirming that MoSe$_2$ assisted by PVP were successfully exfoliated and expanded, derived from that the PVP insertion reduced the interlayer Van der Waals forces. After the carbonization treatment, the hybrid nanosheets could deliver an improved Li/Na-storage performance. Through the analysis of Raman spectra in Fig. 1c, the peak (marked as A$_{1g}$) is the exclusive peak of MoSe$_2$ 2H structure, whilst the peaks (donated as E$_{2g}^1$, J$_2$) are the characteristic peaks for 1T peaks.[17] Thus, it is concluded that PMS and CMS are composed of 1T/2H phases, and the existed 1T phase would increase metallic properties of MoSe$_2$, which is beneficial for electrochemical properties.[18] Moreover, it is expected for PMS, that its peak at 240

cm^{-1} was shifted to the lower wavenumbers, and that its peak at 280 cm^{-1} moves towards the higher wavenumbers, demonstrating the few-layered MoSe$_2$ were effectively formed. [18-20] Evidentially, the peaks assigned to carbon at 1300 and 1500 cm^{-1} are found for PMS. The carbon content of PMS is quantified by TG as shown in Fig. 1d, and the residual product (MoO$_3$) is verified in the inset of Fig. 1d. Clearly, this increasing part is attributed to some of MoSe$_2$ transforming into MoO$_3$ and SeO$_2$, showing the carbon content to be determined to be ~10.8 wt %.

In order to explore the chemical composition and state, PMS is analyzed by XPS. Fig. 2 and Fig. 1S prove the presence of M cvo, Se, C, O, N elements. From the Mo core level XPS spectra in Fig. 2a, it is found that PMS is composed of 1T/2H MoSe$_2$. 2H-MoSe$_2$ is associated with peaks at 232.1 and 229 eV and 1T-MoSe$_2$ is relation with the peaks at 231.8 and 229.2 eV, agreeing well with the analysis of Raman. Meanwhile, the content of 1T MoSe$_2$ is calculated to be 60.3%. Surprisingly, the Mo (6+) peaks with binding energy is found, which demonstrates the existence of C-O-Mo.[9, 21] Note that, the peak at 237 eV confirmed the existence of C-O-Mo bonds that is beneficial to stabilize the volume expansion and give a faster rate of electron transfer. It is deduced that the C-O-Mo comes from the carbonyl (-C=O) of PVP connected with Mo ions. Fig. 2 displayed two couples of peaks for Se 3d. The peaks located at 54 eV, 56 eV are about 3d$_{5/2}$ and 3d$_{3/2}$, respectively. Moreover, as shown in Fig. 2c, the peaks of C1s spectra at 287.8, 285.5, 284.6, 283.3 eV are associated with C=O, C-OH/C-O-Mo, Csp2 and C-H. Through the deconvolution of

the high-resolution spectrum O1s spectra, three peaks were obtained at 532.5, 531.3, 530.5 eV, corresponding to the vibration of C=O, C-O-Mo, O-OH bonds. It is deduced that the Mo atoms at the edge of few-layer $MoSe_2$ connected with O atoms from the PVP to obtain a stabilized C-O-Mo bond, which could inhibit the destruction of the structure.

To better understand the nature of the C-O-Mo bond, the first-principles calculations have been performed based on the simplified C-O-Mo interface models (as presented in Figure 3), which were assembled by the simplified models of oxidized-graphene, $MoSe_2$ sheet fragment and oxidized-C60 fullerene (as given in Figure 2S). The calculations offered some valuable parameters (bond length, bond order, bonding energy, HOMO and LUMO), which are related to the electrochemical performance of a given structure. Frontier molecular orbitals (HOMO and LUMO) were found to be extremely valuable in the interpretation of relevant chemical reactivity. The capacity of a molecule to donate electrons is highly correlated with the HOMO. HOMO also governs the spatial distribution of valence electron mainly participating in the formation of chemical bonds, and LUMO plays an important role in explain the capacity of a molecule to accept electrons.[22] Furthermore, The HOMO-LUMO energy gap (denoted as ΔE_{gap}) between the highest occupied molecular orbital (HOMO) and the lowest unoccupied molecular orbital (LUMO) is a valuable parameter for examining the kinetic stability of a molecule. Larger the energy gap is, better is the stability of the material. On the other hand, the binding energy of a given molecule determines its thermodynamic stability.[23]

Figure 3b demonstrated S-type interface model structures in which oxidized-graphene (ox- graphene) is perpendicular to the plane of $MoSe_2$ sheet. Here,

it should be mentioned that in the present work, Mo, Se, C, O, H atoms are represented as small balls and colored in light blue, yellow, dark gray, red and white, respectively. It is obvious from Figure 3b to see that B3LYP and ωB97XD give very similar molecular structures for the S-type interface model. The distribution of frontier orbitals from ωB97XD calculation is also analogous to that observed from B3LYP calculation. Both HOMO and LUMO are mainly localized on the MoSe$_2$ sheet, suggesting that the interfaces structure will remain the excellent conductibility of MoSe$_2$ nanometer material. As listed in Table 1. The HOMO-LUMO gaps calculated by B3LYP and ωB97XD are 0.72 eV and 3.74 eV, respectively. ωB97XD included dispersion correction and could give a better electronic structure. Thus, the HOMO-LUMO gap of S-type interface model was believed to be 3.74 eV here. It suggested the interface structure would possess good conductivity and nice kinetic stability.

On the other hand, as shown in Table 1S, the bonding energy of Mo-O in the simplified S-type interface model is -37.3 kcal/mol from ωB97XD calculation, which is more negative than that from B3LYP calculation by 16.2 kcal/mol. However, the first-principles DFT calculations with B3LYP and ωB97XD consistently predicated that Mo-O was thermodynamically favorable. Furthermore, DFT calculations with B3LYP and ωB97XD obtain very similar bond length and bond order. As displayed in Table 2S, The C-O bond length in the optimized S-type interface structure is 1.394 Å (1.388 Å) from B3LYP (ωB97XD) calculation, which is just slightly different from the value 1.382 Å (1.374 Å) in the optimized ox-graphene. The Mo-O bond length (2.103 Å) from B3LYP is almost the same with that (2.100 Å) from ωB97XD, which is close to the Mo-O bond length (1.990 Å) in Tugarinovite (MoO$_2$).[24, 25] The C-O bond

order in the optimized S-type interface structure is 0.830 (0.829) from B3LYP (ωB97XD), which is little smaller than that of 0.914 (0.915) in the optimized ox-graphene structure.

All these facts consistently indicated that the S-type interface structure was stable both thermodynamically and kinetically. The similar conclusions could be also derived for L-type interface model and C_{60}-O-Mo interface model. A very interesting finding is that the three simplified interfaces models give very similar HOMO-LUMO gap, C-O (Mo-O) bond length and bond order, which implied the unique C-O-Mo bond should make the hybrid materials possess a general performance (good stability and excellent conductivity). The similar results also co-support that the proposed interface models are reasonable.

The nanostructure of the CMS/FMS/PMS were analyzed by TEM, HRTEM, SAED and Mapping as shown in Fig. 4. Clearly, the large sheets of CMS, the hollow spheres of FMS and the nanospheres of PMS in Fig. 4A1-C1 are consistence well with the results of SEM (Fig. 3S). Orderly stacking of the multi-large-layers is the main constitution of the CMS structure, which reduces the mechanical stress and electron mobility.[26, 27] The relative homogeneity of PMS is observed, which is crucial for an excellent electrode material. In Fig. 4A2, some fragments attached to the surface of CMS, perhaps leading to a reduced electrochemical performance. The thin wall of FMS hollow sphere is only 35.2 nm, which would facilitate the infiltration of electrolyte and alleviate the volume expansion to some extent. Note that, the surface of PMS nanospheres is rough and contain plenty of structural defects, ensuring the availability of plentiful active sites. According to the previous report,[28]

13

the rate capacity is relation with the interparticle diffusion, which is ascribed to that lacking time renders less active sites take part in the reaction. However, the small particles would bring the surface sites distributed in a wider range of energy, which is attributed to their various energy levels. The wide distribution of active sites would be beneficial for improving the electrochemical properties of conversion-based battery materials. In Fig. 4A3-C3, the detailed structure and phase were explored through HRTEM images. It is obvious that owing to the good crystallinity, CMS shows the clear hexagonal honeycomb structure with three Se atoms surrounded one Mo atom. The lattice spacing is about 0.28 and 0.23nm, corresponding to the (100), (103) faces of 2H-$MoSe_2$.[29, 30] In case of FMS, some 1T-$MoSe_2$ phases are observed through that of six Se atoms bonded to one Mo atom in the partial region of the lattice fringe.[31] Note that, the nature of 1T $MoSe_2$ is metallic, facilitating the ions transferring. Moreover, the d-spacing (0.68 nm) is assigned to the (002) planes ($MoSe_2$, JCPDS Card, No. 29-0914), and the large lattice distance in the electrolyte could provide more entrances for Li/Na-insertion/extraction.[3, 32] Expected that the (002) interlayer of the $MoSe_2$ is successfully expanded with the assistance of the PVP, and the interlayer distance reaches to 0.90 nm in Fig. 4C3. The graphitic carbon (the d(002) of carbon, 0.34 nm) was wrapped with few-layer $MoSe_2$, which would improve the conductivity and significantly prolong the cycling stability through the utilization of potentially harmful by-products (Se, demonstrated in the following).[33] Importantly, the carbon decorated upon the lattice face was found, which originates

from the formation of C-O-Mo between the carbonyl group (from PVP) and host Mo ions. By the comparison of their SAED images, the usual hexagonal spot pattern for CMS was clearly due to the well crystalline structure. The diffraction rings of the FMS and PMS are indexed to (002), (105) and (220) for $MoSe_2$, and that of carbon (002) is displayed in Fig. 4C4. Moreover, the elemental mappings of PMS nanosphere reveal the homogenous distribution of C, N, Mo, Se in the host structure. The structure merits of PMS, containing the unique morphology and N-doping graphite, would promote cycling stability and large rate capacity of electrode materials.[10]

The cycling capability of the as-prepared samples was explored at 1.0 A g^{-1} between 3.0 and 0.01V as shown in Fig. 5a and 4S. PMS could deliver a high initial discharge/charge capacities of 1183 and 896 mAh g^{-1} with a coulombic efficiency (CE) of 75.7%, whilst the CMS and FMS exhibited 773/595 mAh g^{-1} with a CE of 76.9% and 442/651 mAh g^{-1} with 68.9%, respectively. The irreversible capacity is due to the adverse reaction and the formation of SEI film. After 150 cycles, the Li-storage capacity of CMS/FMS/PMS remained 176, 341, 1208 mAh g^{-1}, and that of PMS is larger than those of previous works in Table 2. Impressively, the capacity of PMS increases gradually, that of FMS has a rise before 100 cycles but fading subsequently, and that of CMS has continuously decreased. For the continuously fading of CMS, the insulator Se-O film formed on the surface of anodes, coming from that Se ions reacted with the carbonate solvent, [34, 35] which would prevent the transportation of ions. For the increasing part of FMS/PMS, the *in-situ* generated selenide participates in the

electrochemical reaction as the active materials.[10] For the decreasing part for FMS, overmuch Se was dissolved in the electrolyte, further deteriorating the ether-based electrolyte.[36, 37] From their differential charge capacity plots (DCPs) at 100 cycles, it is found that the peaks of CMS nearly disappear, which is ascribed to the loss of electrode activity, resulted from the serious pulverization and adverse reactions. A couple of primary reduction/oxidation peaks were located at ~ 1.9/2.2V, and the voltage difference of FMS/PMS is 0.44V, 0.29V, suggesting that the wrapped carbon plays a crucial role in the structure stabilization. According to the previous report,[10] the generation of Se was expressive, and the detailed reaction process should be illustrated clearly. For discharge process, Se is first reduced to Li_2Se_n (n>4), further to Li_2Se_2 and Li_2Se, corresponding to the peaks at 2.0 and 0.8V. For charge process, Li_2Se is oxidized into insoluble intermediate polyselenides Li_2Se_n (n ≥ 4) and Se, where the peaks located at 1.5 and 2.2 V.[34, 35] In the DCPs of PMS at different curves for Fig. 5c, the growing peak intensity of selenium-lithiation/delithiation is obvious, adequately confirming that the content of Se is increasing upon cycling, which results in the promotion of the capacity. Moreover, in Fig. 5c, the rate stabilities for PMS were improved and the good cycling stability was displayed over the whole period. After 200 cycles, the charge capacity retained 801, 519, 453 and 277 mAh g^{-1} at 2.0, 4.0, 6.0 and 8.0 A g^{-1}, respectively, which reveals superior large-rate cycling stability. Moreover, it is found that the increasing tendency is decreasing with the improvement of current densities, which is due to that there is not enough time for

lithium ions reacting with electroactive sites, leading to the reduction of in-generated selenium.[28] The rate properties of the electrode samples, as the important criteria for practical application, were investigated at stepwise current densities as exhibited in Fig. 5e. Clearly, PMS delivers capacity of 1203, 1064, 956 and 865 mAh g^{-1} at 0.2, 0.5, 1.0 and 5.0 A g^{-1}, whilst CMS and FMS display the unsatisfied performances. And the remained capacities of CMS/FMS/PMS are 1026, 188 and 78 mAh g^{-1} after all the cycles. Considering the aforementioned issues, it is concluded that the layer-by-layer carbon and C-O-Mo bonds of PMS effectively stabilize structure as well as constrain the *in-situ* generated Se.[35, 38] Attracted by the increasing properties of PMS, the detailed analysis was carried out. In the initial 175 cycles at 2.0 A g^{-1}, the capacity of PMS grew to ~800 mAh g^{-1}, and it remained stable in the following 25 loops, which is due to that the in-situ generated Se reached to the maximum value. Fig. 5g displays the similar charge/discharge platforms of PMS at 180th, 185th, 190th, 195th and 200th, suggesting the stable electrochemical reaction without extra Se generation. In Fig. 5f, the charge platforms of PMS at 2.0 A g^{-1} at different cycles were shown. It is found that the platforms at 2.0 V are stable, meanwhile, the platforms at 1.5 V become clear gradually , indicating that the in-situ generated Se participates in the electrochemical reaction. Fig. 5h displays the histogram of Li-storage capacity at various cycles. Obviously, the content of the in-generated Se at every cycles is almost same, and the selenium could deliver a capacity of 283 mAh g^{-1}. The similar cycling behaviors were displayed at 4.0, 6.0, 8.0

A g^{-1}, and their Li-storage capacity would remain stable in the final loops.

Further understanding of the enhanced electrochemical properties were next explored.

The Na-storage properties were analyzed between 0.01 and 3.0 V (Figure. 6). As

clearly shown in Fig. 6a, the initial capacity of PMS was ~ 498/689 mAh g^{-1} with a

CE of 72.7% at 0.1 A g^{-1}. After the activation process before 25 cycles, the rise of

capacity was observed subsequently, similar to Li-storage behaviors. After 120 cycles,

the capacity of PMS increases to 552.1 mAh g^{-1}, higher than those of previous reports

as summarized in Table 2. Meanwhile, PMS with the hollow structure still kept a

capacity of 403.9 mAh g^{-1}, but that of CMS is only 242.9 mAh g^{-1}, further revealing

the importance of structure design. By the comparison of discharge/charge platforms

at 100 cycles in Fig. 6e, their voltages were increased in the order of CMS > FMS >

PMS, indicating the facile electrochemical reaction for PMS. Accompanying with the

charge-discharge process, the Se atoms of chain-like Se would form a stronger

interaction with the carbon substrate, thereby constrained in the carbon layer. From

the rate capability in Fig. 6b, the excellent property of PMS was exhibited, delivering

a capacity of 417, 390, 367, 353 and 339 mAh g^{-1} at 0.1, 0.2, 0.5, 1.0, 2.0 and 5.0 A

g^{-1}, respectively. When the current density reduced to 0.1 A g^{-1}, a capacity of 518 mAh

g^{-1} is still recovered. With the cycling at 1.0 A g^{-1}, its capacity is about 491 mAh g^{-1} at

100th cycle. Fig. 6c presents the comparison of large-current cycling stability for

CMS/FMS/PMS, where the capacity of PMS can reach to 529 mAh g^{-1} after 120

cycles at 1.0 A g^{-1}, which is ascribed to its stable structure and *in-situ* generated Se. In

Fig. 5S, the longer cycling of PMS was displayed and the maximum capacity could reach to ~ 570 mAh g^{-1}, and it kept stable in the following cycles (from 200th to 250th). The capacity of FMS kept stability before 80 cycles and fades subsequently, resulted from the destruction of the structure coming from fast Na-insertion/extraction and the dissolution of selenium. Moreover, from the *ex-situ* SEM of the electrodes and separators over 100 cycles in Fig. 5S, it is obvious that the small size of particle facilitates samples stable upon the Cu foils, which is beneficial for the electrochemical properties. Over the whole period, it is clear that the capacity of PMS kept at ~ 446, 348, 261 and 244 over current densities of 2.0, 4.0, 6.0 and 8.0 A g^{-1}, and this increasing capacity phenomenon is stilled observed. With the increasing of current densities, the growth tendency of capacity is reducing, agreeing well with the Li-storage behaviors. Through the comparison of DCPs at 2nd, 30th, 60th 100th cycles, the rising capacity region was mainly located at 2.0 ~ 3.0 V. Recent report demonstrates that Se was produced in ~ 2.3V for MoSe$_2$, which is corresponding to the reaction ($Na_2Se + 2e^- \rightarrow 2Na + Se$), which was further demonstrated by *ex-situ* XRD in Fig. 7S. [10] Effectively confined by the carbon shell with C-O-Mo bonds, the *in-situ* generated Se plays multi-roles expected roles for the MoSe$_2$ materials: (1) the active materials for the high capacity; (2) the conductive agent for the rate performance. [33, 39] Moreover, the electrochemical properties of commercial pure selenium for LIBs/SIBs were investigated and displayed in Fig. 6S. It is obvious that the cycling were fading seriously without the protection of effective carbon layer

The point that the *in-situ* generated Se leads to the increasing capacity was further supported and evaluated in the Fig. 7. As clearly exhibited in Fig. 7a for the charge curves of different cycles (2nd, 20th, 40th, 60th, 80th, 100th, 120th), the curves below 1.8V are close to overlapping, whilst those in the range of 1.8 - 3.0 V are gradually flat, indicating that the rising capacity derives from the electrochemical reaction above 1.8 V. Thus, the capacity in different voltage ranges were exhibited in Figure. 7(b), the capacity contributions for different cycles between 0.01 and 1.8 V keep constant and remain at ~250 mAh g^{-1}, but those above 1.8 V increase from 173 to 265 mAh g^{-1}. Two reasons can be concluded: (1) the capacity from host conversion reaction ($Na_2Se + Mo + 2e^- \rightarrow 2Na + MoSe_2$) is almost same, indicating the stable Na-capacity contribution of $MoSe_2$; (2) the portion from the emerging conversion reaction ($Na_2Se + 2e^- \rightarrow 2Na + Se$) is increasing, indicating that more in-generated Se participate the sodiation/desodiation reactions upon repeated cycling. The contribution of the Se is about 92 mAh g^{-1}, approaching to 20 % of total capacity, which activate PMS take part in the electrochemical reaction completely. The CV curves at the scan rate of 5.0 mV s^{-1} were displayed in Fig. 7(c). The gradually enlarged areas agree well with the cycling performance. Owing to two kinds of conversion reactions, the reduction peaks at 1.5 V slowly separated into two peaks. Meanwhile, the oxidation peak at ~2.3 V appeared more distinctly and moved towards high voltages, demonstrating that new substance was generated in the high oxidation region. The *ex-situ* Raman spectra of PMS after different cycles present a clear

evolution of the Se. The broad peak at 250 cm^{-1} appears, which are indexed to amorphous Se comprised of Se$_n$ chain at 252 cm^{-1}.[37, 40] With cycling, the intensity of peak becomes strong, representing the augmentation of Se hybrid. Note that, a strong interaction was produced between carbon substrate and the chain-like Se$_n$, successfully confining Se in the carbon matrix, which is in favor of improving the cycling stability and rate capability.[31]

Fig. 8 demonstrates the *ex-situ* TEM, HRTEM, SAED of PMS after recharging to 3.0 V at the 100th Na-insertion/extraction cycle at 0.1 A g^{-1}, clearly revealing the variations of structure and components. As clearly exhibited in Fig. 8, the structure of CMS has a serious pulverization. Meanwhile, the hollow structure of FMS effectively alleviated the volume swelling, but some fragments were still observed. The stable structure of PMS was observed, which further demonstrates its advantages of the designed structure. In Fig. 8A2-C2, the emergence of a large shadow was found for CMS and these shadowed dots were distributed in the fragments of FMS, implying that the by-products (containing Se, Mo) from the MoSe$_2$ are aggregated seriously. By contrast, no obvious dots were found for PMS, which suggests that the by-products Se were uniformly confined in the carbon. In the HRTEM images, the calculated lattice distance of FMS is ~ 0.70 nm, which is assigned to the (002) face of the MoSe$_2$. And the enlarged lattice fringes are attributed to the expansion resulted from the insertion of Na$^+$. In Fig. 8A3, the lattice for the Mo structure is not detected but confirmed through the weak diffraction ring of Mo (226), which was ascribed to the losing of

Mo-containing ions in the electrolyte. Expectedly, in Fig. 8B3, the lattice fringes with a d-distance (0.21 nm) corresponds to the (226) planes of Mo (JCPDs Card: 88-2331), which reveal that some Se from $MoSe_2$ were produced.[10] Importantly, the Se was detected to scatter homogeneously in the carbon matrix, confirming that carbon layer effectively confined the Se, which is beneficial for improving capacity and conductivity. For the SAED images of PMS in Fig. 8C4, the presence of diffraction rings about Mo (226), $MoSe_2$ (002), (100) and (220) is the evidence of generated Mo, and $MoSe_2$. It is concluded that the similar reaction for the as-obtained electrodes, but the rational design of the structure is vital for confining the *in-situ* generated Se.

In Fig. 9, the CV curves of PMS and FMS as LIBs/SIBs batteries were displayed. Clearly, the first cycle is distinctly different from other cycles, which is ascribed to the formation of SEI (solid electrolyte interface) film and some side reactions. In Fig. 9A1, A2, CV curves of PMS/FMS as LIBs anodes at 0.1 mV s^{-1} were shown and it is found that 2nd and 3rd curves keep consistence, suggesting the cycling stability at initial part. In the comparison of their 3rd cycles in Fig. 9. A3, the appeared peak of FMS at 1.5 V is relation with the phase transform ($Li_2Se \rightarrow Li_2Se_n + Se$).[34] And the other peak ($Li_2Se \rightarrow Li_2Se_n + Se$) at 2.2 V maybe overlapped with the peak (Li_2Se with Mo was converted to $MoSe_2$). Meanwhile, the peak of PMS at 1.5 V is not clear, demonstrating that the C-O-Mo bonds could promote the reversible conversion at initial cycling.[21] Obviously, in Fig. 9B1, B2, the position of redox peaks were shifted to low voltage, resulted from the sluggish sodium kinetic. The peak at 2.26 V

22

is due to the *in-situ* generated Se, which has been demonstrated by the previous report, [10] illustrating that the reversible conversion for SIBs is uncontrolled by C-O-Mo bonds. According to the key work,[1] the Se could be further stabilized in the carbon matrix. Note that the peak of PMS is broadened as compared to that of FMS. The phenomenon was rationally illustrated.[28] Theoretically, the equal active sites would require the same energy, giving rise to a sharp peak. However, the electroactivity of sites is distributed in a range, resulting the wide peak. With the reduction of particle size, the increased electroactive sites would lead to the broad distribution of redox site energies. Obviously, the competition between the neighboring redox centers to participate in the redox reaction would be less, which could improve charge/discharge rate. It is concluded that the decreasing particle is the fundamental reason for high-rate performance.

For further investigating the interfacial properties of the PMS, EIS was carried out to evaluate the evolution of surface as displayed in Fig. 9B and Fig. 9S. From the initial Nyquist plots of the as-obtained samples in Fig. 9S, the curve is composed of two parts: (1) the depressed semicircles in the high frequency corresponds to the active materials/electrolyte resistance; (2) a slow line at low frequency is relation with the Warburg impedance. The smaller particles with a larger area connecting with electrolyte could lessen the resistance, and the existing carbon leads to the further reduction of resistance. The subsequent EIS (the 20th and 80th cycles for LIBs, the 10th and 40th for SIBs) are shown with fitting line as well as corresponding equivalent

circuit modeling in Fig. 9B2 and B3, revealing the similar interfacial behavior. Obviously, owing to the better kinetic coefficient of Li$^+$, the smaller resistance is clearly exhibited compared to that for SIBs. And the drastically decreasing resistance demonstrates the formation of by-products, which could enhance electronic conductivity. Moreover, after some cycles, the EIS curves exhibit two depressed semicircles in the high and middle frequency middle, suggesting the emerging of new interfacial resistance. According to the excellent fitting lines, the equivalent circuit modeling is available, in which R$_1$ is the electrolyte resistance form the bulk, separator, electrode, R$_2$ is about the charge transfer resistance in the carbon shell and SEI film interface/electrolyte for PMS (S1, [R2, CPE1]), R3 is the charge transfer resistance in the interface of MoSe$_2$ grains/electrolyte (S2, [R3, CPE2]). Through the simplified models of PMS in Fig. 9B3, the interfacial resistance between carbon and materials was illustrated clearly, whilst the function of the emerging intermediates can be observed directly. In this model, the carbon/electrolyte interfacial and the interfacial SEI electrolyte interfacial are defined S1. The electrolyte that infiltrates in the internal structure of PMS through the plentiful defects and microporous, could form the S2 interface that composed of Se, Se-O species.[39] Owing to the improved conductivity from the *in-situ* generated Se, the impendences were decreased, whilst the diffusion coefficients were increased gradually in Fig. 10S. All the fitting data of EIS are recorded in Table 3 and Fig. 11S, and the Faradic current density (I$_F$) of S1 and the diffusion coefficient (D) of PMS are calculated, obeying the following

Equation 1–3.

$$Z = R + \sigma w^{-0.5} \tag{1}$$

$$I_F = RT/nAFR_2 \tag{2}$$

$$D = 0.5\, R^2 T^2/S^2 n^4 F^4 C^2 \sigma^2 \tag{3}$$

Clearly, with cycling, the value R2 of resistance reduced from 52 to 33 Ω for LIBs, 191 to 57 Ω for SIBs, accompanied by its space charge capacitance CPE1 dropping from 3.8×10^{-4} to 1.7×10^{-4} F for LIBs, 1.6×10^{-4} to 1.1×10^{-4} F for SIBs, resulted from that more charge aggregated at interface S1 would reduce the resistance. Moreover, the value of I_F increases from 3.29×10^{-4} to 7.41×10^{-4} mA cm^{-2} for LIBs, 8.55×10^{-5} to 3.28×10^{-4} mA cm^{-2}. Based upon the previous report, the formation of dense and complete SEI film would improve the conductivity of interfacial carrier, which is beneficial for the generation of pseudo-capacitance during the Li$^+$/Na$^+$ insertion/extraction.[41] Furthermore, the reduction of D as recorded in Table 3 and Fig. 11S demonstrate that the emerging by-products possess the high conductivity, facilitating the fast electron transfer. Note that, the formation of dual-capacitive interface would be in favor of the charge accumulation on the interface, inducing the deep insertion the host structure and increasing the diffusion ability of Li$^+$/Na$^+$ ions, thereby improving the electrochemical performances.[42]

4. Conclusion

In summary, the exfoliated MoSe$_2$ constrained inside C nanospheres with the uniform diameter of 100 nm were successfully prepared through the assistance of the dual

roles of PVP, bringing the large lattice distance of (002) face and few-layers structure. The first-principles DFT calculations predicted that the unique C-O-Mo bond should make the hybrid materials possess general performance (good stability and excellent conductivity). Utilized as anodes for LIBs/SIBs, besides the stable capacity of host materials $MoSe_2$, the significant design with C-O-Mo binding would act an important role in anchoring and activating the *in-situ* generated of Se, effectively lowering the adverse reaction, accompanying with the improved capacity stability and rate properties. For LIBs, after cycling, the capacity can be kept about 801, 549 mAh g^{-1} at 2.0, 4.0 A g^{-1}, respectively. For SIBs, the remained capacity is about 441, 348 mAh g^{-1} at 1.0, 4.0 A g^{-1} after 120 cycles. *Ex-situ* Raman and HRTEM confirmed that the as-formed Se is restrained by the effective structure, which is distributed homogeneously through the chain-like Se_n molecule strongly interacted with the carbon. Through the quantitative analysis of CV and EIS, the reduction of particle size with *in-situ* generate Se could improve the charge-discharge rate and conductivity of dual-capacitive, which are deemed as the fundamental reason for the excellent electrochemical properties. This work opens up a wide avenue to the design of 2D TMDs as anodes for LIBs/SIBs, and enhances in-depth understanding of the effect about the *in-situ* generated Se on the energy-storage behaviors of metal-selenide, whilst bringing new investigating strategy on the metal-based materials.

Appendix A. Supporting information

Supplementary data associated with this article can be found in the online at ***

Reference

[1] A. Eftekhari, The rise of lithium–selenium batteries, Sustainable Energy & Fuels, 1 (2017) 14-29.

[2] A. Eftekhari, Molybdenum diselenide ($MoSe_2$) for energy storage, catalysis, and optoelectronics, Applied Materials Today, 8 (2017) 1-17.

[3] W. Tang, D. Xie, T. Shen, X. Wang, D. Wang, X. Zhang, X. Xia, J. Wu, J. Tu, Construction of Nitrogen-Doped Carbon-Coated $MoSe_2$ Microspheres with Enhanced Performance for Lithium Storage, Chemistry, 23 (2017) 12924-12929.

[4] J. Wang, C. Peng, L. Zhang, Y. Fu, H. Li, X. Zhao, J. Zhu, X. Wang, Construction

of N-doped carbon@$MoSe_2$ core/branch nanostructure via simultaneous formation of core and branch for high-performance lithium-ion batteries, Electrochim. Acta., 256 (2017) 19-27.

[5] T. Chen, Z. Zhang, B. Cheng, R. Chen, Y. Hu, L. Ma, G. Zhu, J. Liu, Z. Jin, Self-Templated Formation of Interlaced Carbon Nanotubes Threaded Hollow Co_3S_4 Nanoboxes for High-Rate and Heat-Resistant Lithium-Sulfur Batteries, J. Am. Chem. Soc., 139 (2017) 12710-12715.

[6] H. Wang, L. Wang, X. Wang, J. Quan, L. Mi, L. Yuan, G. Li, B. Zhang, H. Zhong, Y. Jiang, High Quality $MoSe_2$ Nanospheres with Superior Electrochemical Properties for Sodium Batteries, J. Electroanal. Chem., 163 (2016) A1627-A1632.

[7] B. Chen, Y. Meng, F. He, E. Liu, C. Shi, C. He, L. Ma, Q. Li, J. Li, N. Zhao, Thermal decomposition-reduced layer-by-layer nitrogen-doped graphene/MoS_2/nitrogen-doped graphene heterostructure for promising lithium-ion batteries, Nano Ener., 41 (2017) 154-163.

[8] F. Niu, J. Yang, N. Wang, D. Zhang, W. Fan, J. Yang, Y. Qian, $MoSe_2$-Covered N,P-Doped Carbon Nanosheets as a Long-Life and High-Rate Anode Material for Sodium-Ion Batteries, Adv. Funct. Mater., 27 (2017) 1700522.

[9] T. Xiang, S. Tao, W. Xu, Q. Fang, C. Wu, D. Liu, Y. Zhou, A. Khalil, Z. Muhammad, W. Chu, Z. Wang, H. Xiang, Q. Liu, L. Song, Stable 1T-$MoSe_2$ and Carbon Nanotube Hybridized Flexible Film: Binder-Free and High-Performance Li-Ion Anode, ACS Nano, 11 (2017) 6483-6491.

[10] F. Niu, J. Yang, N. Wang, D. Zhang, W. Fan, J. Yang, Y. Qian, $MoSe_2$-Covered N,P-Doped Carbon Nanosheets as a Long-Life and High-Rate Anode Material for Sodium-Ion Batteries, Adv. Funct. Mater., 27 (2017).

[11] X. Zhang, Z. Lai, C. Tan, H. Zhang, Solution-Processed Two-Dimensional MoS_2 Nanosheets: Preparation, Hybridization, and Applications, Angew. Chem. Int. Ed., 55 (2016) 8816-8838.

[12] C. Dai, Z. Zhou, C. Tian, Y. Li, C. Yang, X. Gao, X. Tian, Large-Scale Synthesis

of Graphene-Like $MoSe_2$ Nanosheets for Efficient Hydrogen Evolution Reaction, J. Phys. Chem. C, 121 (2017) 1974-1981.

[13] Z. Lei, W. Zhu, S. Xu, J. Ding, J. Wan, P. Wu, Hydrophilic $MoSe_2$ Nanosheets as Effective Photothermal Therapy Agents and Their Application in Smart Devices, ACS Appl. Mater. Interfaces., 8 (2016) 20900-20908.

[14] S. Zhang, J. Li, E. Wang, Ultrafine transition metal dichalcogenide nanodots prepared by polyvinylpyrrolidone-assisted liquid phase exfoliation, J. Mater. Chem. B, 5 (2017) 2609-2615.

[15] J. Liu, Z. Zeng, X. Cao, G. Lu, L.H. Wang, Q.L. Fan, W. Huang, H. Zhang, Preparation of MoS_2-polyvinylpyrrolidone nanocomposites for flexible nonvolatile rewritable memory devices with reduced graphene oxide electrodes, Small, 8 (2012) 3517-3522.

[16] Y. Cao, L. Xiao, M.L. Sushko, W. Wang, B. Schwenzer, J. Xiao, Z. Nie, L.V. Saraf, Z. Yang, J. Liu, Sodium ion insertion in hollow carbon nanowires for battery applications, Nano Lett, 12 (2012) 3783-3787.

[17] B. Xia, T. Wang, W. Xiao, R. Zhang, P. Liu, J. Ding, D. Gao, D. Xue, Phase-transfer induced room temperature ferromagnetic behavior in 1T@2H-$MoSe_2$ nanosheets, Sci. Rep., 7 (2017) 45307.

[18] J.B. Cook, H.-S. Kim, Y. Yan, J.S. Ko, S. Robbennolt, B. Dunn, S.H. Tolbert, Mesoporous MoS_2 as a Transition Metal Dichalcogenide Exhibiting Pseudocapacitive Li and Na-Ion Charge Storage, Adv. Energy Mater., 6 (2016) 1501937.

[19] M. Zhuang, Y. Ding, X. Ou, Z. Luo, Polymer-confined growth of perforated $MoSe_2$ single-crystals on N-doped graphene toward enhanced hydrogen evolution, Nanoscale, 9 (2017) 4652-4659.

[20] M.-H. Wu, J.-T. Lee, Y.J. Chung, M. Srinivaas, J.-M. Wu, Ultrahigh efficient degradation activity of single- and few-layered $MoSe_2$ nanoflowers in dark by piezo-catalyst effect, Nano Ener., 40 (2017) 369-375.

[21] X. Zhao, H.-E. Wang, Y. Yang, Z.G. Neale, R.C. Massé, J. Cao, W. Cai, J. Sui, G.

Cao, Reversible and fast Na-ion storage in $MoO_2/MoSe_2$ heterostructures for high energy-high power Na-ion capacitors, Energy Storage Mater., 12 (2018) 241-251.

[22] P. Chen, Y. Hu, Z. Gao, J. Zhai, D. Fang, T. Yue, C. Zhang, W. Sun, Discovery of a Novel Cationic Surfactant: Tributyltetradecyl-Phosphonium Chloride for Iron Ore Flotation: From Prediction to Experimental Verification, Minerals, 7 (2017) 240.

[23] L.P. Ding, F.H. Zhang, Y.S. Zhu, C. Lu, X.Y. Kuang, J. Lv, P. Shao, Understanding the structural transformation, stability of medium-sized neutral and charged silicon clusters, Sci. Rep., 5 (2015).

[24] M.G. Brik, I. Sildos, V. Kiisk, First-principles calculations of optical and electronic properties of pure and Sm^{3+}-doped TiO_2, Physica B-Condensed Matter, 405 (2010) 2450-2456.

[25] R.T. Downs, M. Hall-Wallace, The American mineralogist crystal structure database, American Mineralogist, 88 (2003) 247-250.

[26] G. Li, D. Luo, X. Wang, M.H. Seo, S. Hemmati, A. Yu, Z. Chen, Enhanced Reversible Sodium-Ion Intercalation by Synergistic Coupling of Few-Layered MoS_2 and S-Doped Graphene, Adv. Funct. Mater., 27 (2017).

[27] X. Li, Y. Yang, J. Liu, L. Ouyang, J. Liu, R. Hu, L. Yang, M. Zhu, MoS_2/cotton-derived carbon fibers with enhanced cyclic performance for sodium-ion batteries, Applied Surface Science, 413 (2017) 169-174.

[28] A. Eftekhari, M. Mohamedi, Tailoring pseudocapacitive materials from a mechanistic perspective, Mater. Today Energy, 6 (2017) 211-229.

[29] Y. Gong, G. Ye, S. Lei, G. Shi, Y. He, J. Lin, X. Zhang, R. Vajtai, S.T. Pantelides, W. Zhou, B. Li, P.M. Ajayan, Synthesis of Millimeter-Scale Transition Metal Dichalcogenides Single Crystals, Adv. Funct. Mater., 26 (2016) 2009-2015.

[30] M.K. Cheng, J. Liang, Y.H. Lai, L.X. Pang, Y. Liu, J.Y. Shen, J.Q. Hou, Q. Lin He, B.C. Xu, J.S. Chen, G. Wang, C. Liu, R. Lortz, I.K. Sou, Large-area epitaxial growth of MoSe2 via an incandescent molybdenum source, Nanotechnology, 28 (2017) 455601.

[31] X. Wang, X. Shen, Z. Wang, R. Yu, L. Chen, Atomic-Scale Clarification of Structural Transition of MoS_2 upon Sodium Intercalation, Acs Nano, 8 (2014) 11394-11400.

[32] J. Li, H. Hu, F. Qin, P. Zhang, L. Zou, H. Wang, K. Zhang, Y. Lai, Flower-like $MoSe2$ /C Composite with Expanded (002) Planes of Few-layer $MoSe_2$ as the Anode for High-Performance Sodium-Ion Batteries, Chemistry, 23 (2017) 14004-14010.

[33] J. Ding, H. Zhou, H. Zhang, T. Stephenson, Z. Li, D. Karpuzov, D. Mitlin, Exceptional energy and new insight with a sodium–selenium battery based on a carbon nanosheet cathode and a pseudographite anode, Energy Environ. Sci., 10 (2017) 153-165.

[34] Y. Cui, A. Abouimrane, J. Lu, T. Bolin, Y. Ren, W. Weng, C. Sun, V.A. Maroni, S.M. Heald, K. Amine, (De)lithiation mechanism of Li/SeS_x (x = 0-7) batteries determined by in situ synchrotron X-ray diffraction and X-ray absorption spectroscopy, J. Am. Chem. Soc., 135 (2013) 8047-8056.

[35] A. Abouimrane, D. Dambournet, K.W. Chapman, P.J. Chupas, W. Weng, K. Amine, A new class of lithium and sodium rechargeable batteries based on selenium and selenium-sulfur as a positive electrode, J. Am. Chem. Soc., 134 (2012) 4505-4508.

[36] H. Zhang, D. Jia, Z. Yang, F. Yu, Y. Su, D. Wang, Q. Shen, Alkaline lignin derived porous carbon as an efficient scaffold for lithium-selenium battery cathode, Carbon, 122 (2017) 547-555.

[37] C.-P. Yang, S. Xin, Y.-X. Yin, H. Ye, J. Zhang, Y.-G. Guo, An Advanced Selenium-Carbon Cathode for Rechargeable Lithium-Selenium Batteries, Angew. Chem. Int. Ed., 52 (2013) 8363-8367.

[38] K. Han, Z. Liu, J. Shen, Y. Lin, F. Dai, H. Ye, A Free-Standing and Ultralong-Life Lithium-Selenium Battery Cathode Enabled by 3D Mesoporous Carbon/Graphene Hierarchical Architecture, Adv. Funct. Mater., 25 (2015) 455-463.

[39] C. Luo, Y. Xu, Y. Zhu, Y. Liu, S. Zheng, Y. Liu, A. Langrock, C. Wang,

Selenium@Mesoporous Carbon Composite with Superior Lithium and Sodium Storage Capacity, Acs Nano, 7 (2013) 8003-8010.

[40] H. Ye, Y.-X. Yin, S.-F. Zhang, Y.-G. Guo, Advanced Se–C nanocomposites: a bifunctional electrode material for both Li–Se and Li-ion batteries, J. Mater. Chem. A, 2 (2014) 13293.

[41] T. Xia, W. Zhang, J. Murowchick, G. Liu, X. Chen, Built-in Electric Field-Assisted Surface-Amorphized Nanocrystals for High-Rate Lithium-Ion Battery, Nano Letters, 13 (2013) 5289-5296.

[42] H. Huang, S. Gao, A.-M. Wu, K. Cheng, X.-N. Li, X.-X. Gao, J.-J. Zhao, X.-L. Dong, G.-Z. Cao, Fe_3N constrained inside C nanocages as an anode for Li-ion batteries through post-synthesis nitridation, Nano Ener., 31 (2017) 74-83.

[43] C. Cui, G. Zhou, W. Wei, L. Chen, C. Li, J. Yue, Boosting sodium-ion storage performance of $MoSe_2$@C electrospinning nanofibers by embedding graphene nanosheets, J. Alloys Compd., 727 (2017) 1280-1287.

[44] R. Jin, Y. Cui, Q. Wang, G. Li, Facile fabrication of CNTs@C@$MoSe_2$@Se hybrids with amorphous structure for high performance anode in lithium-ion batteries, J. Colloid Interface Sci., 508 (2017) 435-442.

[45] G. Jia, H. Wang, D. Chao, H. He, N.H. Tiep, Y. Zhang, Z. Zhang, H.J. Fan, Ultrathin $MoSe_2$@N-doped carbon composite nanospheres for stable Na-ion storage, Nanotechnology, 28 (2017) 42LT01.

[46] C. Zheng, C. Chen, L. Chen, M. Wei, A CMK-5-encapsulated $MoSe_2$ composite for rechargeable lithium-ion batteries with improved electrochemical performance, J. Mater. Chem. A, 5 (2017) 19632-19638.

[47] G.D. Park, J.H. Kim, S.K. Park, Y.C. Kang, $MoSe_2$ Embedded CNT-Reduced Graphene Oxide Composite Microsphere with Superior Sodium Ion Storage and Electrocatalytic Hydrogen Evolution Performances, ACS Appl Mater Interfaces, 9 (2017) 10673-10683.

[48] D. Xie, X. Xia, Y. Zhong, Y. Wang, D. Wang, X. Wang, J. Tu, Exploring

Advanced Sandwiched Arrays by Vertical Graphene and N-Doped Carbon for Enhanced Sodium Storage, Adv. Energy Mater., 7 (2017).

[49] Y. Tang, Z. Zhao, Y. Wang, Y. Dong, Y. Liu, X. Wang, J. Qiu, Carbon-Stabilized Interlayer-Expanded Few-Layer $MoSe_2$ Nanosheets for Sodium Ion Batteries with Enhanced Rate Capability and Cycling Performance, ACS Appl Mater Interfaces, 8 (2016) 32324-32332.

[50] X. Yang, Z. Zhang, X. Shi, Rational design of coaxial-cable $MoSe_2$/C: Towards high performance electrode materials for lithium-ion and sodium-ion batteries, J. Alloys Compd., 686 (2016) 413-420.

[51] X. Zhao, J. Sui, F. Li, H. Fang, H. Wang, J. Li, W. Cai, G. Cao, Lamellar $MoSe_2$ nanosheets embedded with MoO_2 nanoparticles: novel hybrid nanostructures promoted excellent performances for lithium ion batteries, Nanoscale, 8 (2016) 17902-17910.

[52] B. Mendoza-Sánchez, J. Coelho, A. Pokle, V. Nicolosi, A study of the charge storage properties of a $MoSe_2$ nanoplatelets/SWCNTs electrode in a Li-ion based electrolyte, Electrochim. Acta., 192 (2016) 1-7.

[53] Z. Luo, J. Zhou, L. Wang, G. Fang, A. Pan, S. Liang, Two-dimensional hybrid nanosheets of few layered $MoSe_2$ on reduced graphene oxide as anodes for long-cycle-life lithium-ion batteries, J. Mater. Chem. A, 4 (2016) 15302-15308.

[54] H. Wu, Y. Wu, X. Chen, Y. Ma, M. Xu, W. Wei, J. Pan, X. Xiong, Rational design and preparation of few-layered $MoSe_2$ nanosheet@C/TiO_2 nanobelt heterostructures with superior lithium storage performance, RSC Adv., 6 (2016) 23161-23168.

[55] S.H. Choi, Y.C. Kang, Fullerene-like $MoSe_2$ nanoparticles-embedded CNT balls with excellent structural stability for highly reversible sodium-ion storage, Nanoscale, 8 (2016) 4209-4216.

[56] Z. Zhang, Y. Fu, X. Yang, Y. Qu, Z. Zhang, Hierarchical $MoSe_2$ Nanosheets/Reduced Graphene Oxide Composites as Anodes for Lithium-Ion and Sodium-Ion Batteries with Enhanced Electrochemical Performance, ChemNanoMat, 1

(2015) 409-414.

[57] Y.Y. Lee, G.O. Park, Y.S. Choi, J.K. Shon, J. Yoon, K.H. Kim, W.-S. Yoon, H. Kim, J.M. Kim, Mesoporous transition metal dichalcogenide ME_2 (M = Mo, W; E = S, Se) with 2-D layered crystallinity as anode materials for lithium ion batteries, RSC Adv., 6 (2016) 14253-14260.

[58] Y. Zhang, Z. Liu, H. Zhao, Y. Du, $MoSe_2$ nanosheets grown on carbon cloth with superior electrochemical performance as flexible electrode for sodium ion batteries, RSC Adv., 6 (2016) 1440-1444.

[59] H. Wang, X. Lan, D. Jiang, Y. Zhang, H. Zhong, Z. Zhang, Y. Jiang, Sodium storage and transport properties in pyrolysis synthesized $MoSe_2$ nanoplates for high performance sodium-ion batteries, J. Power Sources., 283 (2015) 187-194.

[60] J. Yao, B. Liu, S. Ozden, J. Wu, S. Yang, M.-T.F. Rodrigues, K. Kalaga, P. Dong, P. Xiao, Y. Zhang, R. Vajtai, P.M. Ajayan, 3D Nanostructured Molybdenum Diselenide/Graphene Foam as Anodes for Long-Cycle Life Lithium-ion Batteries, Electrochim. Acta., 176 (2015) 103-111.

[61] L. Ma, X. Zhou, L. Xu, X. Xu, L. Zhang, W. Chen, Ultrathin few-layered molybdenum selenide/graphene hybrid with superior electrochemical Li-storage performance, J. Power Sources., 285 (2015) 274-280.

[62] H. Wang, X. Wang, L. Wang, J. Wang, D. Jiang, G. Li, Y. Zhang, H. Zhong, Y. Jiang, Phase Transition Mechanism and Electrochemical Properties of Nanocrystalline $MoSe_2$ as Anode Materials for the High Performance Lithium-Ion Battery, J. Phys. Chem. C, 119 (2015) 10197-10205.

[63] X. Yang, Z. Zhang, Y. Fu, Q. Li, Porous hollow carbon spheres decorated with molybdenum diselenide nanosheets as anodes for highly reversible lithium and sodium storage, Nanoscale, 7 (2015) 10198-10203.

[64] Y. Yang, S. Wang, J. Zhang, H. Li, Z. Tang, X. Wang, Nanosheet-assembled $MoSe_2$ and S-doped $MoSe_{2-x}$ nanostructures for superior lithium storage properties and hydrogen evolution reactions, Inorg. Chem. Front., 2 (2015) 931-937.

[65] Y. Liu, M. Zhu, D. Chen, Sheet-like MoSe$_2$/C composites with enhanced Li-ion storage properties, J. Mater. Chem. A, 3 (2015) 11857-11862.

[66] Y.N. Ko, S.H. Choi, S.B. Park, Y.C. Kang, Hierarchical MoSe$_2$ yolk-shell microspheres with superior Na-ion storage properties, Nanoscale, 6 (2014) 10511-10515.

[67] Y. Shi, C. Hua, B. Li, X. Fang, C. Yao, Y. Zhang, Y.-S. Hu, Z. Wang, L. Chen, D. Zhao, G.D. Stucky, Highly Ordered Mesoporous Crystalline MoSe$_2$ Material with Efficient Visible-Light-Driven Photocatalytic Activity and Enhanced Lithium Storage Performance, Adv. Funct. Mater., 23 (2013) 1832-1838.

Figures and Captions

Figure. 1 The schematic diagram (a), FTIR spectra of $MoSe_2$/PVP before annealing (b), XRD patterns (c) and Raman spectroscopy (d) of CMS/FMS/PMS, and TG curves for PMS (f).

Figure. 2 XPS spectra of Mo 3d (a), Se 3d (b), C 1s (d), and O 1s (e) core level peak regions of PMS.

Figure. 3 (a) S-type interface model (the shorter axis of ox-graphene is perpendicular to the plane of $MoSe_2$ sheet) and its frontier molecular orbitals (HOMO and LUMO), (b) L-type interface model (the longer axis of ox-graphene is perpendicular to the plane of MoSe2 sheet) and its frontier molecular orbitals (HOMO and LUMO), (c) The simplified interface model of $MoSe_2$ sheet on oxidized-fullerene (C_{60}-O-Mo) and its frontier molecular orbitals (HOMO and LUMO).

Fig. 4 TEM, high resolution TEM (HRTEM), selected area diffraction pattern (SAED), elemental mapping images of CMS (A), FMS(B), PMS(C).

Fig. 5 The Li-storage capability: Comparison of the cycling performances (a) at 1.0 A g^{-1} in the potential from 3.0 to 0.01 V, and differential charge vs. voltage curve (dQ/dV) at 100th (b) for those of CMS/FMS/PMS. The rate capability of PMS at different currents (c, e) and dQ/dV of PMS at various cycles (d), the charge platforms (f, g) and the histogram (h) of PMS at 2.0 A g^{-1} at different cycles.

Figure. 6 The Na-storage performances: Comparison of the cycling stability at 0.1 A g^{-1} (a), rate capability at stepwise current densities (b), large-rate cycling properties at

1.0 A g^{-1} (c) for CMS/FMS/PMS, the high-current cycling stabilities of PMS (d), the platforms of the as-made samples after 100 cycles at 0.1 A g^{-1} (e), the DCPs of PMS at 2nd, 30th, 60th and 100th for 2.0 A g^{-1}.

Figure. 7 Comparison of the charge platforms from the 2nd to 120th cycle for PMS at 1.0 A g^{-1} between 3.0 and 0.01 V (a), Reversible charge capacities *vs.* cycles number of PMS electrode separated into the scopes of 0.01 - 1.8 and 1.8 – 1.9 V (b), the cyclic voltammetry (CV) curves from 1st to 120th for PMS (c), the *ex-situ* Raman spectra of the 2nd, 20th, 60th, 100th cycles.

Figure. 8 After 100 charge-discharge cycles at the full charged states, ex-situ TEM, HRTEM, SAED of CMS (A), FMS (B), PMS (C).

Figure. 9. The CV curves of PMS (A1, B1) and FMS (A2, B2) at 0.1 mV s^{-1}, the comparison of CV curves for 3rd cycle as LIBs (A3) and (B3), The 20th and 80th cycles EIS, fitting lines and corresponding equivalent circuit for LIBs (C1), the 10th and 40th cycles EIS, fitting lines and corresponding equivalent circuit for SIBs (C2), the simplified model for the equivalent circuit (C3).

Table. 1 The HOMO-LUMO gaps at different theory levels. Unit is eV.

Table. 2 The electrochemical properties of previous reports about MoSe$_2$ for LIBs/SIBs.
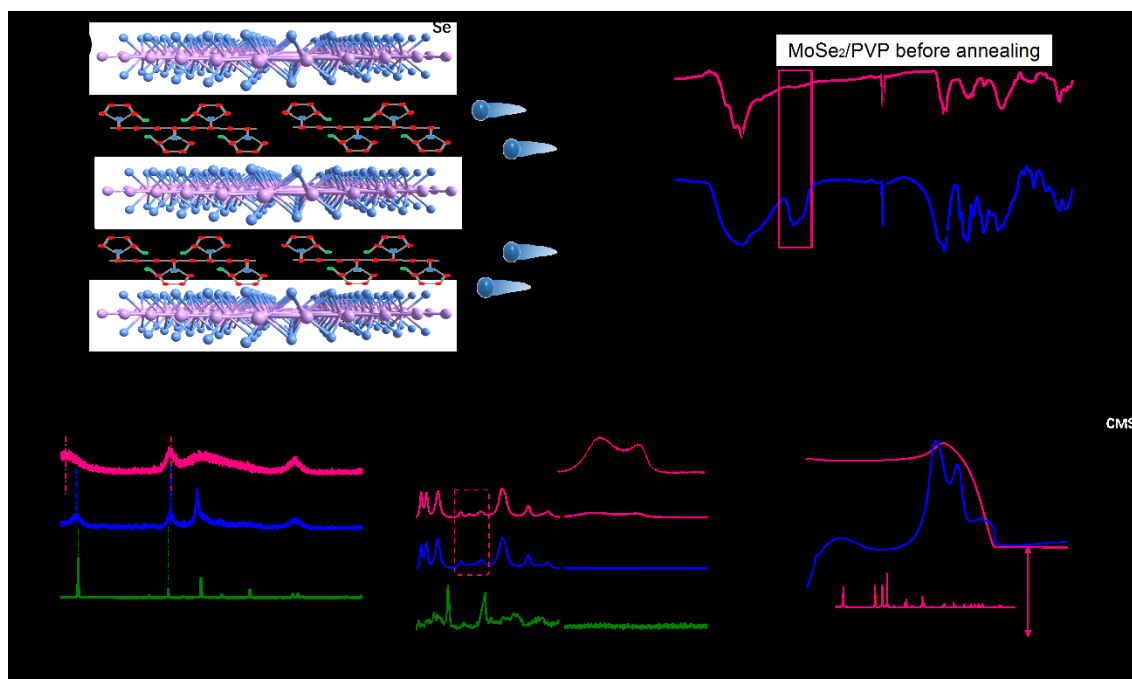
Table. 3 The fitting parameters of PMS.
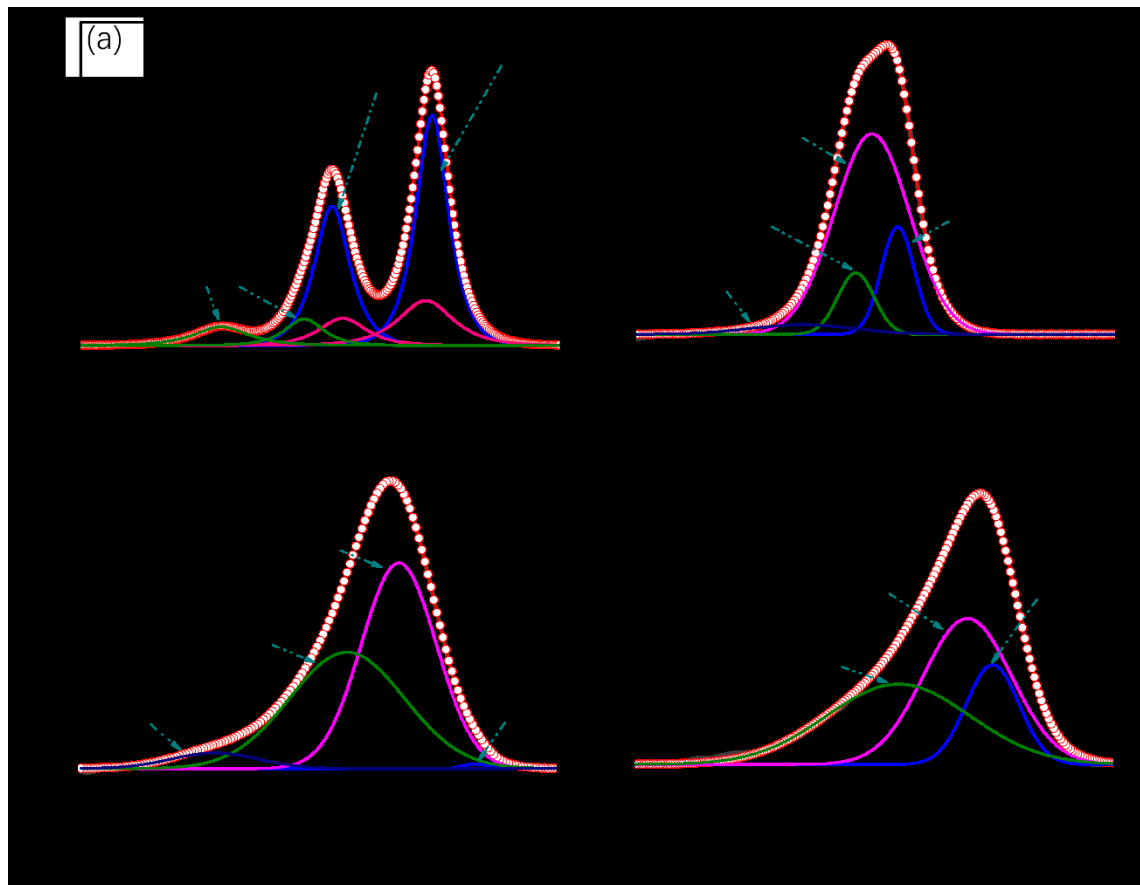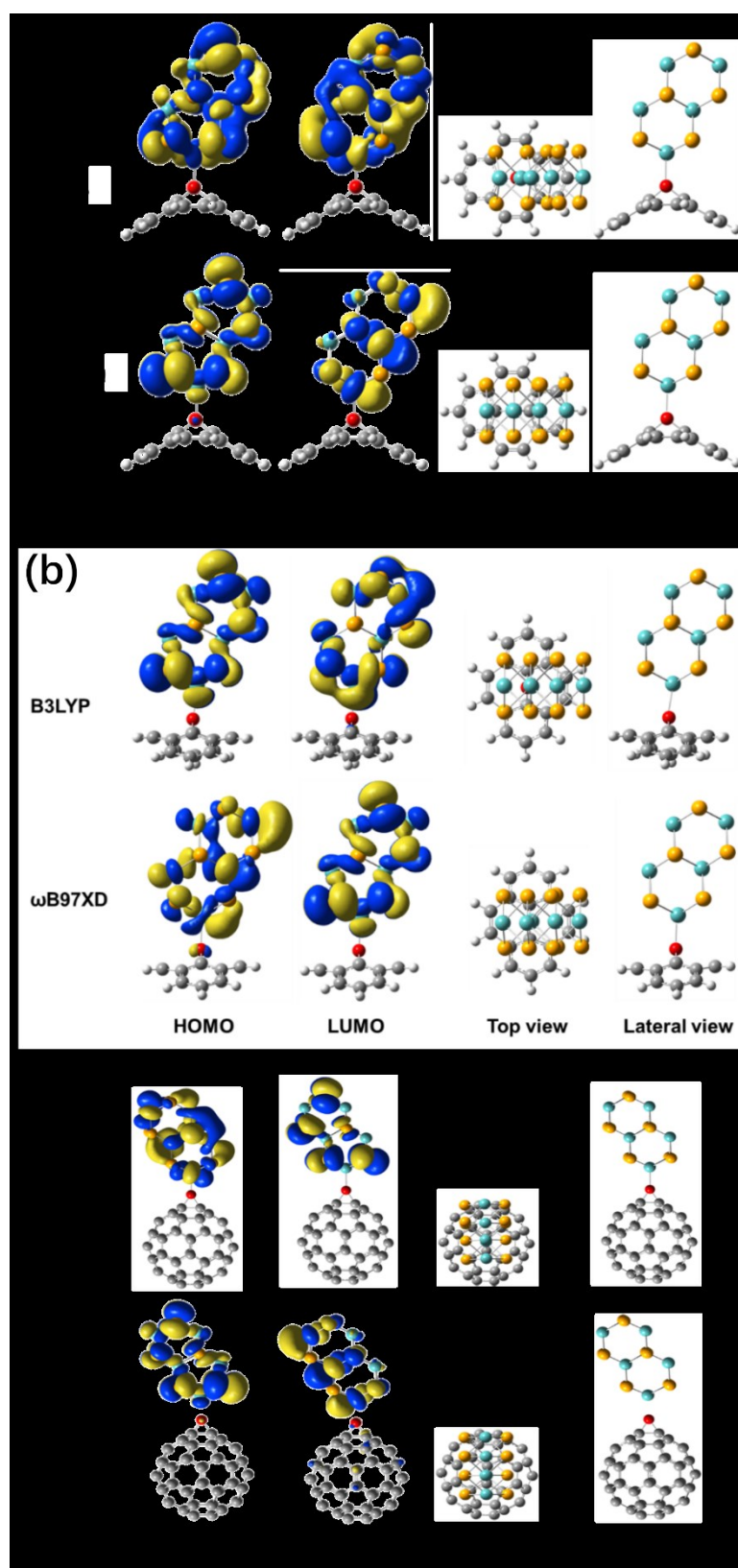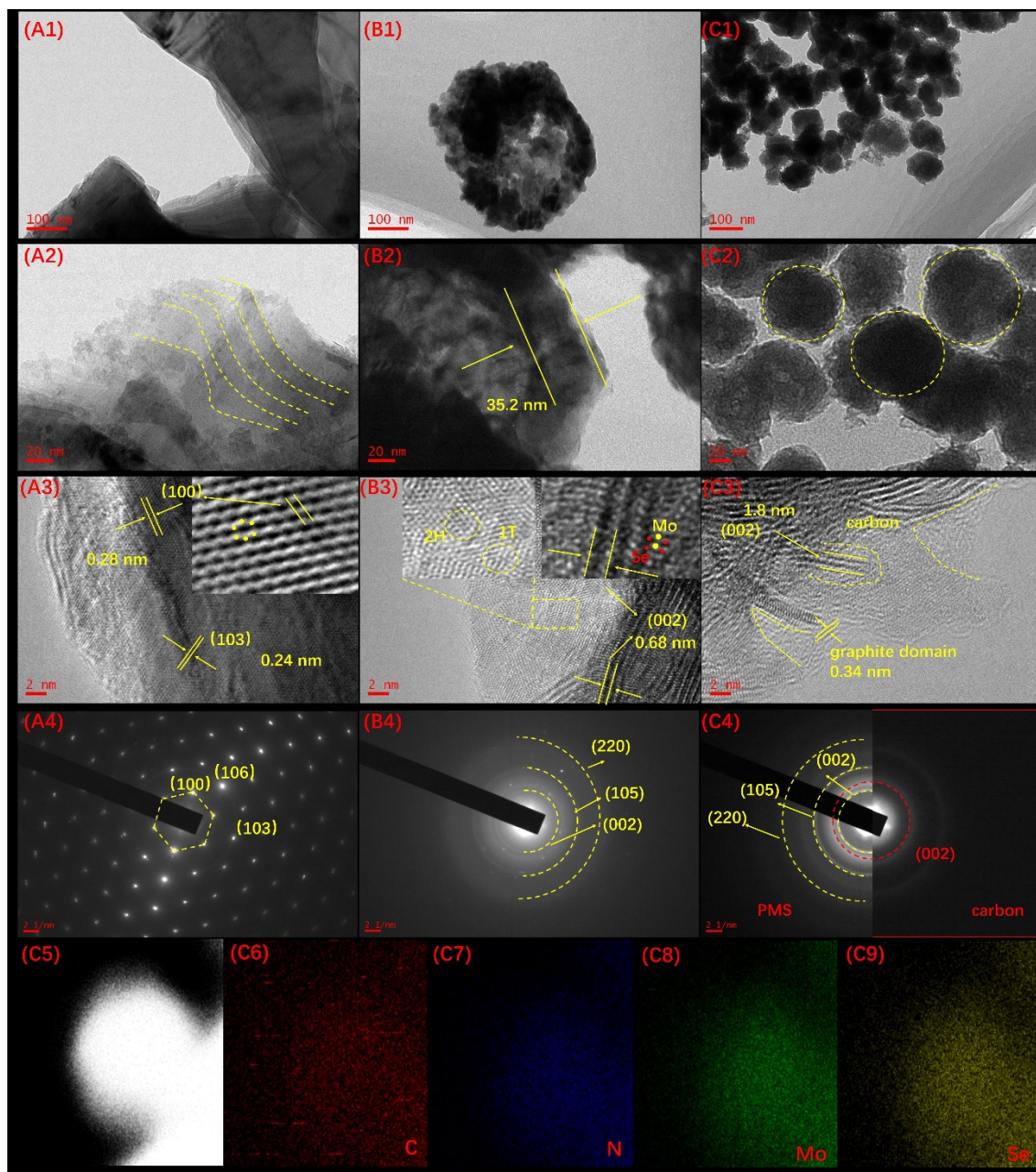
Figure. 1

Figure. 2

Figure. 3

Figure. 4

Figure. 5
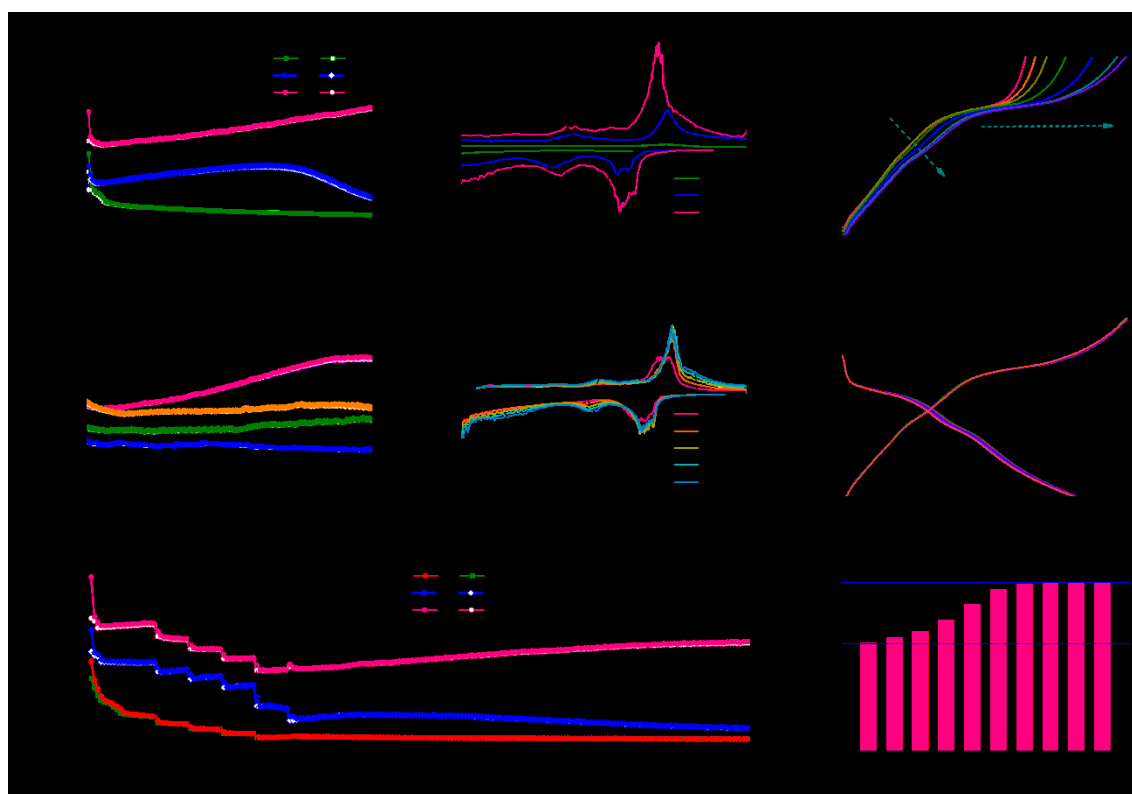
Figure. 6
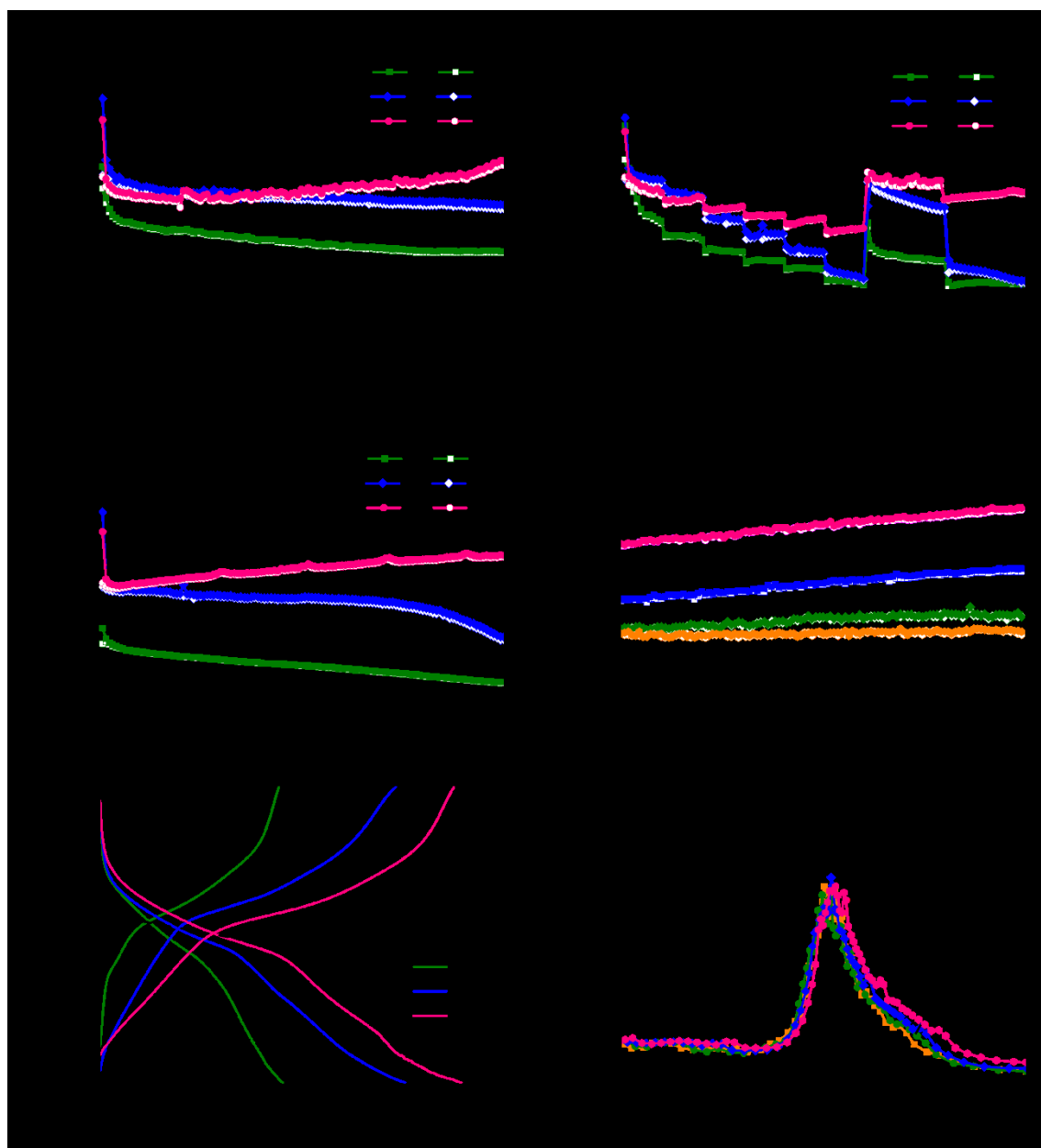
Figure. 7
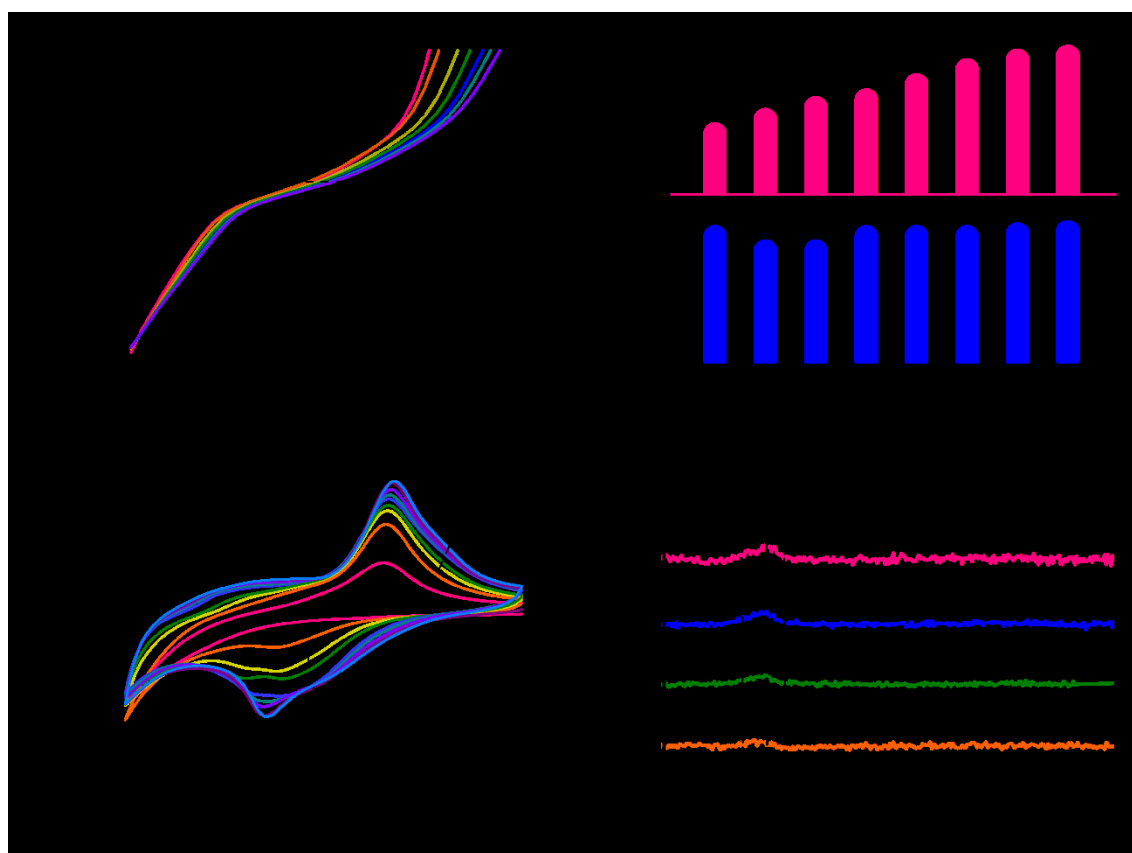
Figure. 8
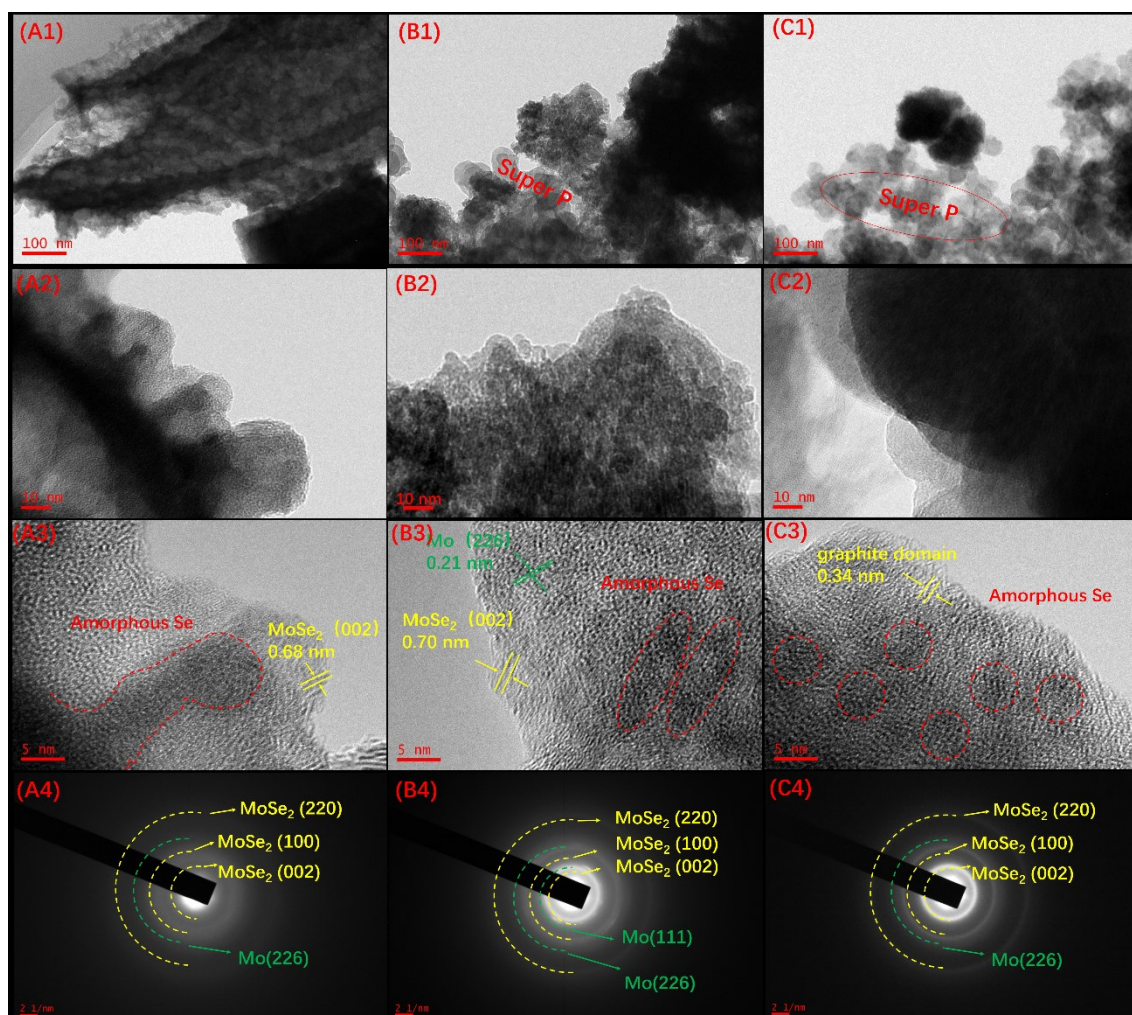
Figure. 9
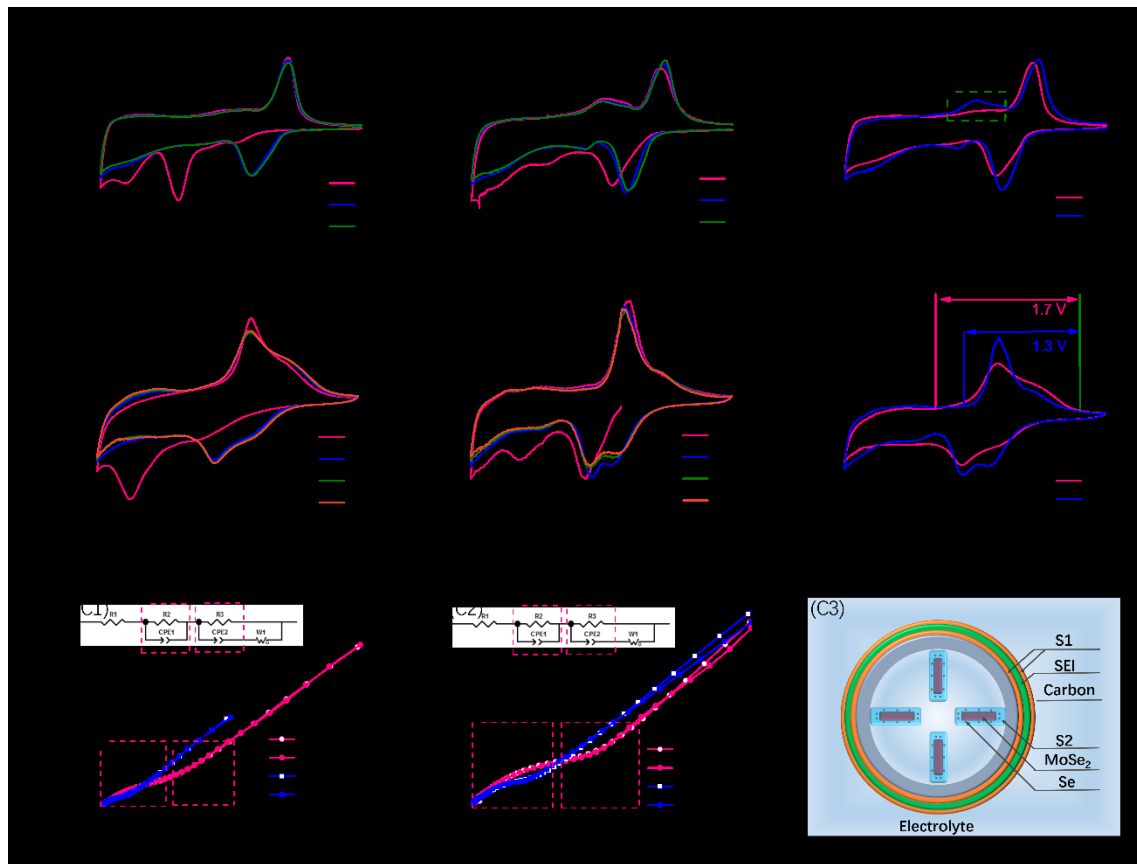
Table 1

Simplified models	B3LYP/6-31G* /LanL2DZ+ECP		ΔE_{gap}	ωB97XD/6-31G* /LanL2DZ+ECP		ΔE_{gap}
	HOMO	LUMO		HOMO	LUMO	
MoSe₂	-5.17	-4.63	0.55	-6.88	-3.07	3.81
ox-graphene	-5.61	-1.41	4.20	-7.46	-0.27	7.17
ox-C60	-5.93	-3.32	2.62	-7.76	-1.96	5.79
S	-4.57	-3.86	0.72	-6.18	-2.42	3.74
L	-4.49	-3.70	0.80	-6.18	-2.29	3.88
C60-O-MoSe2	-4.60	-4.05	0.54	-6.26	-2.53	3.74

Table 2

Materials	Fields	Cycling (mAh g⁻¹)	Rate properties (mAh g⁻¹)	Year/Ref
MoSe₂@N-C nanospheres (100 nm)	Li	1219 after150 cycles at 1.0 A g-1	807 at 2.0 A g⁻¹ 448 at 6.0 A g⁻¹	This work
	Na	552 after 120 cycles at 0.1 A g⁻¹	530 at 1.0 A g⁻¹ 238 at 8.0 A g⁻¹	
MoSe₂@nanofibers	Na	366.9 after 200 cycles at 0.2 A g⁻¹	334.2 at 1.5 A g⁻¹; 320 at 2.0 A g⁻¹	2017[43]
CNTs@C@MoSe₂@Se	Li	1010 after 100 cycles at 0.1 A g⁻¹	508 at 5 A g⁻¹	2017[44]
MoSe₂@N-C	Li	906 after100 cycles at 0.1 A g⁻¹	696 at 0.5 A g⁻¹; 560 at 1.0 A g⁻¹	2017[4]
MoSe2@N-C spheres 0.8um	Na	368 after 500 cycles at 0.5 A g⁻¹	248 at 2.0 A g⁻¹; 180 at 5.0 A g⁻¹	2017[45]
MoSe₂@N-C Microspheres	Li	698 after 100 cycles at 0.1 A g⁻¹	471 at 2.0 A g⁻¹;	2017[3]
MoSe₂@ CMK-5	Li	788 after 100 cycles at 0.1 A g⁻¹	609 at 1.0 A g⁻¹; 542 at 2.0 A g⁻¹	2017[46]
MoSe₂@CNT@Graphene	Na	393 after 200 cycles at1.0 A g⁻¹	314 at 2.0 A g⁻¹; 275 at 5.0 A g⁻¹	2017[47]
Flower-like MoSe₂/C	Na	360 after 350 cycles at 0.5 A g⁻¹	301 at 2.0 A g⁻¹; 266 at 4.0 A g⁻¹	2017[32]
MoSe₂@ N,P - C Nanosheets	Na	378 after 1000 cycles at 0.5 A g⁻¹	351 at 1.0 A g⁻¹; 310 at 5.0 A g⁻¹	2017[8]
1T- MoSe₂ @Carbon Nanotube	Li	971 after 100 cycles at 0.3 A g⁻¹	630 at 3.0 A g⁻¹	2017[9]

Material	Ion	Cyclability	Rate capability	Year[Ref]
MoSe$_2$@N-C Nanosheets	Na	540 after 100 cycles at 0.1 A g^{-1}	298 at 2.0 A g^{-1}	2017[48]
MoSe$_2$ Nanosheets	Na	445 after 100 cycles at 0.1 A g^{-1}	367 at 5.0 A g^{-1}	2016[49]
coaxial-cable MoSe$_2$@C	Li	658 after 100 cycles at 0.5 A g^{-1}	524 at 3.0 A g^{-1}	2016[50]
	Na	423 after 100 cycles at 0.5 A g^{-1}	395 at 1.0 A g^{-1}	
MoO2@MoSe$_2$ heterostructures	Li	~ 1000 after 50 cycles at 0.2 A g^{-1}	726 at 2.0 A g^{-1}	2016[51]
MoSe$_2$@nanoplatelets @SWCNTs	Li	630 after 35 cycles at 0.0315 A g^{-1}	212 at 0.315 A g^{-1}	2016[52]
MoSe$_2$/rGO	Li	715 after 100 cycles at 0.1 A g^{-1}	509 at 1.0 A g^{-1} 436 at 2.0 A g^{-1}	2016[53]
MoSe$_2$ nanosheet@C/TiO2	Li	987 after 100 cycles at 0.5 A g^{-1}	860 at 3.0 A g^{-1}	2016[54]
MoSe$_2$ Nanospheres	Na	344 after 200 cycle at 0.0422 A g^{-1}	212 at 4.22 A g^{-1}	2016[6]
Fullerene-like MoSe2@ CNT balls	Na	296 after 250 cycles at 1.0 A g^{-1}	280 at 3.0 A g^{-1} 255 at 5.0 A g^{-1}	2016[55]
MoSe$_2$ Nanosheets@ rGO	Li	917 after 100 cycles at 0.5 A g^{-1}	750 at 1.0 A g^{-1}	2015[56]
	Na	430 after 200 cycles at 0.5 A g^{-1}	380 at 1.0 A g^{-1}	
Mesoporous MoSe$_2$	Li	728 at 30 cycles at 0.0422 A g^{-1}	~ 500 at 2.0 A g^{-1}	2015[57]
MoSe$_2$@carbon cloth	Na	390 after 100 cycles at 0.2 A g^{-1}	239 at 2.0 A g^{-1} 161 at 5.0 A g^{-1}	2015[58]
MoSe$_2$ nanoplates	Na	369 after 50 cycles at 0.0422 A g^{-1}	250 at 4.22 A g^{-1}	2015[59]
3D MoSe$_2$@Graphene	Li	625 after 100 cycles at 0.0422 A g^{-1}	330 at 0.844 g^{-1}	2015[60]
Few-layered MoSe$_2$@Graphene	Li	1102 after 100 cycles at 0.1 A g^{-1}	454 at 1.0 A g^{-1}	2015[61]

Nanocrystalline MoSe$_2$	Li	405 after 50 cycles at 0.0422 A g^{-1}	322 at 4.22 A g^{-1}	2015[62]
hollow carbon spheres@ MoSe$_2$	Li	681 after 100 cycles at 1.0 A g^{-1}	640 at 3.0 A g^{-1}	2015[63]
hollow carbon spheres@ MoSe$_2$	Na	580 after 100 cycles at 0.2 A g^{-1}	400 at1.5 A g^{-1}	2015[63]
S-doped MoSe$_{2-x}$ nanosheets	Li	947 after 30 cycles at 0.1 A g^{-1}	667 at 0.5 A g^{-1}	2015[64]
Sheet-like MoSe$_2$/C	Li	576 at 50 cycles at 0.1 A g^{-1}	450 at 2.0 A g^{-1}	2015[65]
Hierarchical MoSe$_2$ yolk–shell microspheres	Na	448 after 50 cycles at 0.2 A g^{-1}	345 at 1.5 A g^{-1}	2014[66]
Mesoporous Crystalline MoSe$_2$	Li	630 after 35 cycles at 0.25 A g^{-1}	372 at 0.998 A g^{-1}	2013[67]

Table 3

Samples	CPE1 (F)	CPE2 (F)	R_2 (Ω)	R_3 (Ω)	D (cm^2 s^{-1})	i (mA cm^{-2})
PMS-Li-20th	3.8×10^{-4}	6.7×10^{-4}	52	89	2.26×10^{-16}	3.29×10^{-4}
PMS-Li-80th	1.7×10^{-4}	6.4×10^{-4}	23	39	1.75×10^{-15}	7.41×10^{-4}
PMS-Na-10th	1.6×10^{-4}	9.8×10^{-5}	191	275	4.83×10^{-17}	8.55×10^{-5}
PMS-Na-40th	1.1×10^{-4}	1.5×10^{-4}	57	172	1.56×10^{-16}	3.28×10^{-4}